IJMMM International Journal of Minerals, Metallurgy and Materials 矿物冶金与材料学报（英文版）

Effects of substrate temperature and deposition time on the morphology and corrosion resistance of $FeCoCrNiMo_{0.3}$ high-entropy alloy coating fabricated by magnetron sputtering

Chun-duo Dai, Yu Fu, Jia-xiang Guo, and Cui-wei Du

Cite this article as:
Chun-duo Dai, Yu Fu, Jia-xiang Guo, and Cui-wei Du, Effects of substrate temperature and deposition time on the morphology and corrosion resistance of $FeCoCrNiMo_{0.3}$ high-entropy alloy coating fabricated by magnetron sputtering, *Int. J. Miner. Metall. Mater.*, 27(2020), No. 10, pp. 1388-1397. https://doi.org/10.1007/s12613-020-2149-2

View the article online at SpringerLink or IJMMM Webpage.

International Journal of Minerals, Metallurgy and Materials
Volume 27, Number 10, October 2020, Page 1388
https://doi.org/10.1007/s12613-020-2149-2

Effects of substrate temperature and deposition time on the morphology and corrosion resistance of $FeCoCrNiMo_{0.3}$ high-entropy alloy coating fabricated by magnetron sputtering

Chun-duo Dai[1,2], *Yu Fu*[1,2], *Jia-xiang Guo*[1,2], *and Cui-wei Du*[1,2,3]

1) Institute for Advanced Materials and Technology, University of Science and Technology Beijing, Beijing 100083, China
2) Key Laboratory for Corrosion and Protection, Ministry of Education, Beijing 100083, China
3) Beijing Advanced Innovation Center for Materials Genome Engineering, University of Science and Technology Beijing, Beijing 100083, China
(Received: 6 May 2020; revised: 20 July 2020; accepted: 21 July 2020)

Abstract: The effects of substrate temperature and deposition time on the morphology and corrosion resistance of $FeCoCrNiMo_{0.3}$ coating fabricated by magnetron sputtering were investigated by scanning electron microscopy and electrochemical tests. The $FeCoCrNiMo_{0.3}$ coating was mainly composed of the face-centered cubic phase. High substrate temperature promoted the densification of the coating, and the pitting resistance and protective ability of the coating in 3.5wt% NaCl solution was thus improved. When the deposition time was prolonged at 500°C, the thickness of the coating remarkably increased. Meanwhile, the pitting resistance improved as the deposition time increased from 1 to 3 h; however, further improvement could not be obtained for the coating sputtered for 5 h. Overall, the pitting resistance of the $FeCoCrNiMo_{0.3}$ coating sputtered at 500°C for 3 h exceeds those of most of the reported high-entropy alloy coatings.

Keywords: high-entropy alloy coating; magnetron sputtering; microstructure; corrosion

1. Introduction

Surface coating is an effective method for enhancing the corrosion resistance, wear resistance, and hardness of a metal substrate subjected to a harsh environment [1]. The use of surface coating has been known to improve the durability and service life of structural components. Passive films of about 1–3 nm thickness forming on the surface of alloys for corrosion resistance play a key role in protecting metals from corrosive media [2−4]. Similarly, surface coating technology can be used to protect metal surfaces and is cost-effective. Many types of binary or ternary corrosion-resistant coatings have been developed, and they include metal carbide coatings and metal nitrides or oxide coatings [5−10]. Magnetron sputtering is a widely used deposition technique for fabrication of surface coating [11].

In the past few years, high-entropy alloys (HEAs) with a simple structure and high chemical disorder have attracted much attention due to their surprising and unanticipated combination of properties [12−18]. These HEAs present enormous opportunities and challenges in the design of novel multi-principal coating with outstanding properties [19−21]. HEA coating come in the form of wear-resistant coatings, e.g., $Ni_{0.2}Co_{0.6}Fe_{0.2}CrSi_{0.2}AlTi_{0.2}$ [22] and FeNiCoAlCu [23]; oxidation-resistant coatings, e.g., $NiCo_{0.6}Fe_{0.2}Cr_{1.5}SiAlTi_{0.2}$ [24] and Al−Cr−Nb−Si−Ti [25]; super-hard coatings, e.g., (TiVCrZrNbMoHfTaWAlSi)N [26], (AlCrTaTiZr)NC_y [27], and (AlCrNbSiTiV)N [28]; and coatings with excellent thermal stability [23,29]. The fundamentals of corrosion resistance of HEA coating have been investigated. Ye *et al.* [30] studied the microstructure and corrosion resistance of CrMnFeCoNi HEA coating. They also found that the pitting resistance of the CrMnFeCoNi coating is lower than that of 304 stainless steel (SS) in 3.5wt% NaCl. Li *et al.* [31] deposited FeAlCuCrCoMn HEA coating by direct current magnetron sputtering. Although they obtained a smooth coating, the pitting resistance of the coating is unsatisfactory in 3.5wt% NaCl, and the passive current densities are high in acidic and alkaline solutions. In another work [32], the thermal and corrosion properties of V−Nb−Mo−Ta−W and V−Nb−Mo−Ta−W−Cr−B refractory HEA coatings were studied. V−Nb−Mo−Ta−W−Cr−B alloy exhibits excellent anticorro-

Corresponding author: Cui-wei Du E-mail: dcw@ustb.edu.cn

sion performance, as well as good thermal stability, in 3.5wt% NaCl solution. Nanocrystalline AlTiCrNbTa coating prepared by magnetron sputtering exhibits excellent pitting resistance with high corrosion potential and low passive current density in 3.5wt% NaCl solution [33]. In general, compositional elements affect the corrosion resistance of coating. HEA coating with excellent corrosion resistance can be developed through reasonable compositional design. Moreover, the corrosion resistance of coating strongly depends on its compactness and thickness. According to the literatures [34−37], substrate temperature exerts a significant effect on the microstructure and densification of HEA coating due to the thermal migration of surface adatoms. Meanwhile, deposition time can directly determine the thickness of coating [38−39]. However, the studies related to the effects of deposition parameters on corrosion resistance are limited, thereby restricting the development of anticorrosion HEA coating.

The addition of corrosion-resistant elements, such as Cr, Ni, and Mo, is generally known to improve the corrosion resistance of metals [4,40−44]. In our previous studies and related reports, we found that bulk $FeCoCrNiMo_x$ HEA alloys possess excellent pitting corrosion resistance and passivation performance in NaCl and H_2SO_4 solutions [45−46]. Therefore, we chose to study the effects of substrate temperature and deposition time on the microstructure and corrosion resistance of $FeCoCrNiMo_{0.3}$ coating prepared by magnetron sputtering on a 304 SS substrate using scanning electron microscopy (SEM) and electrochemical tests. The results should pave the way for the development of anticorrosion HEA coating.

2. Experimental

2.1. Sample preparation

A commercially available 304 SS slab (10 mm × 10 mm × 3 mm) was used as the substrate. $FeCoCrNiMo_{0.1}$ coating, which shows lower corrosion resistance than $FeCoCrNiMo_{0.3}$ coating, was also prepared. Herein, the morphology and corrosion resistance of the $FeCoCrNiMo_{0.3}$ coating were investigated. Mo content was controlled by preparing an equiatomic FeCoCrNi alloy in a maglev furnace with high-purity raw materials; pure Mo with diameters of 50.8 and 76.2 mm were used as targets. Radio frequency (RF) and direct current (DC) reactive magnetron sputtering systems were applied to the FeCoCrNi and Mo targets, respectively. Prior to the test, the 304 SS substrates were ground sequentially with SiC papers with 400–2000 grit, polished with 1 μm diamond polishing paste, and then cleaned using alcohol and dried in cold air. The targets were bombarded for 3 min to remove the oxides before sputtering. High-purity Ar gas was filled into a vacuum chamber at 10^{-4} Pa, and the working pressure was maintained at 1 Pa. During the deposition process, most of the Mo target was sheltered by a Q235 plate, and the area of a 10° fraction was exposed after repeated experiments to obtain the $FeCoCrNiMo_{0.3}$ coating. The deposition parameters are listed in Table 1.

Table 1. Deposition parameters of $FeCoCrNiMo_{0.3}$ coating

Substrate temperature / °C	Deposition time / h	Distance / mm	Working pressure / Pa	Bias / V	Exposure angle of Mo target / (°)	DC power / W	RF power / W
200	1	50	1	−400	10	25	180
300	1	50	1	−400	10	25	180
500	1	50	1	−400	10	25	180
500	3	50	1	−400	10	25	180
500	5	50	1	−400	10	25	180

2.2. Morphology and phase

The thickness and chemical compositions of the coatings were characterized with a Quanta 250 scanning electron microscope combined with an energy-dispersive X-ray spectroscopy (EDS) analysis device. The plane-view morphology of the coatings was observed using a Zeiss Supra55 scanning electron microscope. The phase composition was characterized by X-ray diffraction (XRD) (Rigaku, D/max-RB 12 kW) with Cu K_α radiation. The diffraction angles (2θ) varied between 30° and 100° with a step size of 0.02°. The data were analyzed using Jade 5.0 software.

2.3. Electrochemical tests

The electrochemical tests were carried out using the typical three-electrode system with a Pt sheet, saturated calomel electrode, and specimens acting as the auxiliary electrode, reference electrode, and working electrode, respectively. All electrochemical tests were performed on a VersaSTAT 3F workstation. The backside of the specimen without the coating was welded with a wire, and the non-test region was sealed with silicone rubber, thus leaving the area of 10 mm × 10 mm exposed to the solution of 3.5wt% NaCl at pH 6.6. The open-circuit potential (OCP) was recorded for 3600 s to yield a stable state. The dynamic potential polarization curves were measured at a scan rate of 0.5 mV/s from −0.25 V vs. OCP to the final potential corresponding to the current density of 1 mA/cm^2. The electrochemical impedance spectroscopy (EIS) measurements were carried out at a sinusoidal wave voltage of 10 mV and a frequency range of 100 kHz to

10 mHz. The data were fitted using the ZSimpWin software.

3. Results and discussion

3.1. Effect of substrate temperature on the thickness and morphology of the coating

The crystal structures of the $FeCoCrNiMo_{0.3}$ coatings sputtered at different substrate temperatures were confirmed by the XRD patterns (Fig. 1). The main face-centered cubic (fcc) phase was observed and found to have contributed to the high mixing entropy. Considerably few precipitates written as $CrFe_{2.32}MoNi$ were present in the coatings, and they were confirmed to be (Cr,Mo)-rich σ phases [47−48]. Sharp diffraction peaks without preferred orientations were also noted in all the patterns, and they indicated the high crystallinity of the coatings.

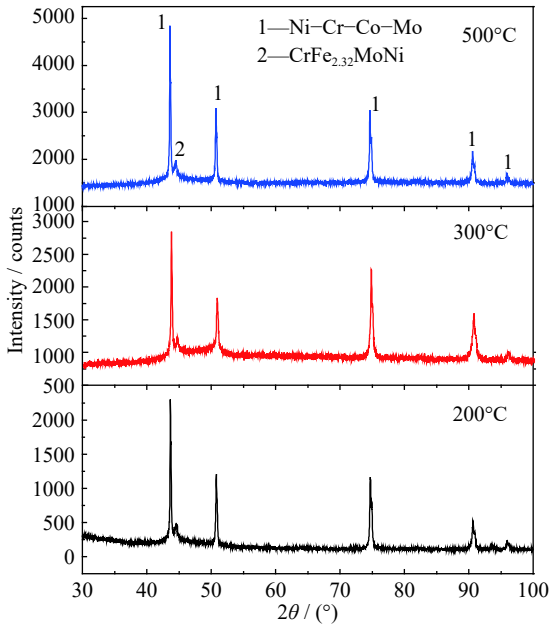

Fig. 1. XRD patterns of $FeCoCrNiMo_{0.3}$ coatings sputtered at 200, 300, and 500°C for 1 h.

The cross-sectional and plane-view images of the $FeCoCrNiMo_{0.3}$ coatings sputtered at 200, 300, and 500°C are shown in Fig. 2. The compositions of the coatings were measured by EDS, and the results are listed in Table 2. As listed in Table 2, the compositions of the coatings sputtered at the three temperatures were all close to the expected ones, thereby indicating that the Fe, Co, Cr, and Ni elements had almost the same sputtering rates under the described deposition parameters [38,49−50]. As observed from Figs. 2(a), 2(c), and 2(e), the thicknesses of the coatings were (884 ± 25), (836 ± 47), and (878 ± 22) nm, respectively. The results demonstrated that the substrate temperature exerted no notable effect on the thickness of the coatings.

Figs. 2(b), 2(d), and 2(f) present the morphologies of the coatings sputtered at 200, 300, and 500°C. Numerous small and equiaxed particles could be seen agglomerated into the islands, which were distributed uniformly on the surface. The size of the islands was reduced greatly, and dense surfaces were observed at 500°C [8,36]. This result could be attributed to the fact that the high kinetic energies of deposited atoms result in a decrease in surface energies at high temperatures and an increase in nucleation or renucleation rates [36,51]; moreover, high temperature promote the diffusion rates of atoms and their migration [51], thereby leading to the formation of dense coating with few microdefects. The densification of coating influences their corrosion resistance, which can be confirmed by electrochemical tests.

3.2. Effect of substrate temperature on the corrosion resistance of the coating

The corrosion resistance of the coatings sputtered at different temperatures was evaluated by dynamic potential polarization measured in 3.5wt% NaCl solution with 304 SS substrate as a reference. As shown in Fig. 3, all coatings exhibited a typical passive behavior. The tendency of pitting and the rate of dissolution of the coating can be depicted by the values of the pitting potential (E_{pit}), corrosion potential (E_{corr}), and corrosion current density (i_{corr}). All values were obtained by Tafel fitting as listed in Table 3. E_{corr} increased with an increase in the substrate temperature, and i_{corr} decreased; notably, E_{pit} of the coating sputtered at 500°C in NaCl solution was much higher than those of the coatings sputtered at lower temperatures and 304 SS. These results revealed that the stability and pitting resistance of these coatings can be improved by raising the substrate temperature.

The protective abilities of the $FeCoCrNiMo_{0.3}$ coatings sputtered at different substrate temperatures were further characterized by EIS. Figs. 4(a) and 4(b) respectively show the Nyquist and Bode plots of the coatings and 304 SS in the testing solution. The Nyquist plots of the coatings sputtered at 300 and 500°C present a single capacitive semicircle with large diameters, indicating high corrosion resistance in the NaCl solution. By contrast, the Nyquist plot of the coating sputtered at 200°C presents a depressed circle. Hence, the protective ability of the coating sputtered at 200°C was considered to be poorer than that of the coatings sputtered at 300 and 500°C. Combined with the fitting results, the EIS spectrum of the coating sputtered at 200°C could be well fitted by the electrical equivalent circuit (EEC) with two time constants, as illustrated in Fig. 4(c). According to previous reports [52−56], two time constants originate in rough coating with microdefects, thus leading to the direct contact between electrolytes and metal substrates during immersion. Thus, the response is caused by the reaction occurring at the electrolyte/metal substrate interface. The EIS spectra of the coatings sputtered at 300 and 500°C could be well fitted by the EEC with one time constant, as illustrated in Fig. 4(d). Accordingly, the coatings sputtered at 300 and 500°C were

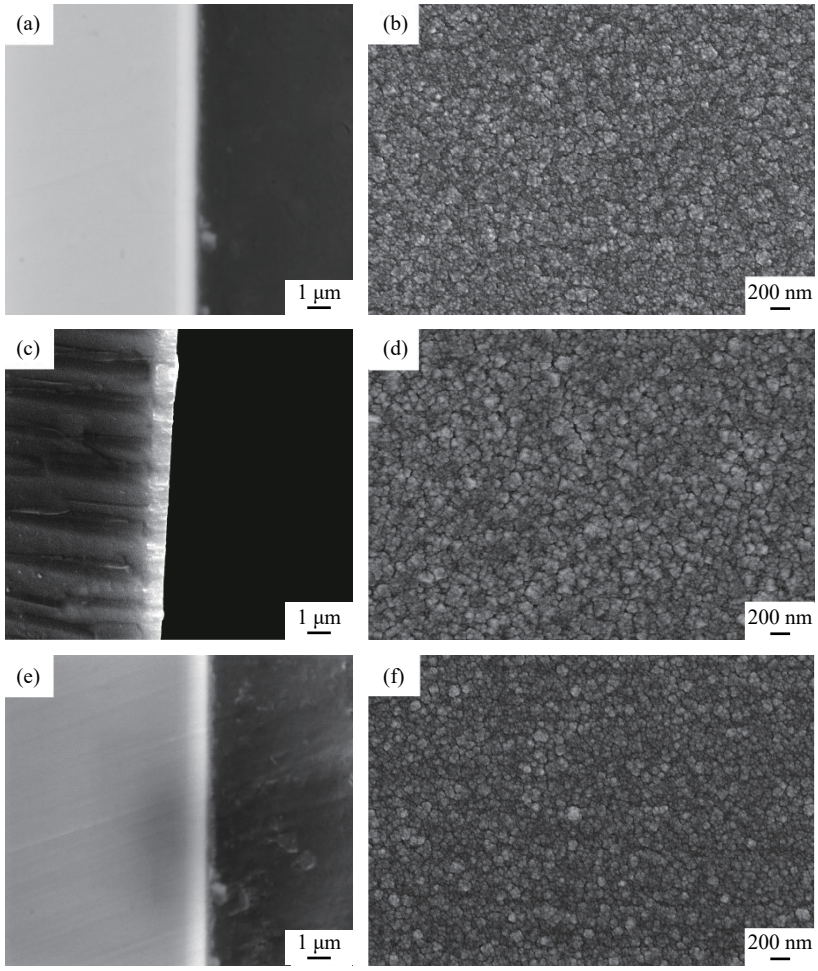

Fig. 2. (a, c, e) Cross-sectional and (b, d, f) plane-view images of $FeCoCrNiMo_{0.3}$ coatings sputtered at different substrate temperatures for 1 h: (a, b) 200°C; (c, d) 300°C; (e, f) 500°C.

Table 2. Thicknesses and chemical compositions of $FeCoCrNiMo_{0.3}$ coatings sputtered at different substrate temperatures for 1 h

Substrate Temperature / °C	Thickness / nm	Content / at%				
		Fe	Co	Cr	Ni	Mo
200	884 ± 25	25.22	23.00	23.10	21.46	7.22
300	836 ± 47	23.55	23.52	23.35	21.71	7.87
500	878 ± 22	23.42	23.17	23.44	21.84	8.13

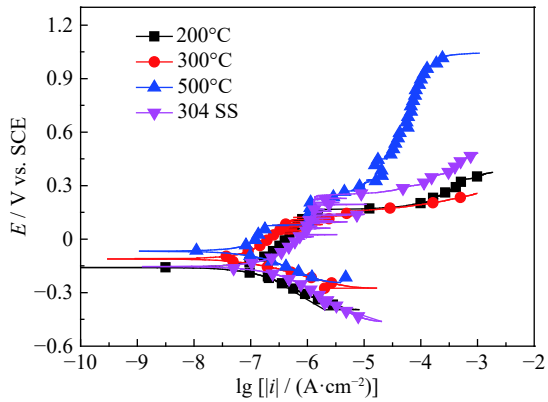

Fig. 3. Dynamic potential polarization curves of $FeCoCrNiMo_{0.3}$ coatings sputtered at different substrate temperatures and 304 SS in 3.5wt% NaCl solution.

compact and free of defects. Thus, the semicircle is merely dominated by a double electrical layer at the solution/coating interface. The EIS spectra further proved that the high substrate temperature improved the quality of the coating.

In both EECs, R_s is the resistance of the solution. In Fig. 4(c), Q_c and R_{el} represent the capacitance of the coating and the resistance of the electrolyte in the defects, respectively; Q_{dl1} and R_{ct} represent the capacitance and charge transfer resistance of the double electrical layer at the electrolyte/metal substrate interface, respectively. The protective properties of the coating depend on the value of $R_{el} + R_{ct}$. In Fig. 4(d), Q_{dl2} and R_p represent the capacitance of the double electrical layer at the solution/coating interface and the polarization resistance contributed by the double electrical layer and coating,

Table 3. Tafel fitting results and pitting potentials obtained from Fig. 3

Specimen	Corrosion potential, E_{corr} / V vs. SCE	Corrosion current density, i_{corr} / (μA·cm^{-2})	Pitting potential, E_{pit} / V vs. SCE
304 SS	–0.1434	0.270	0.3073
200°C	–0.1531	0.084	0.2018
300°C	–0.1052	0.062	0.1926
500°C	–0.0534	0.060	0.8962

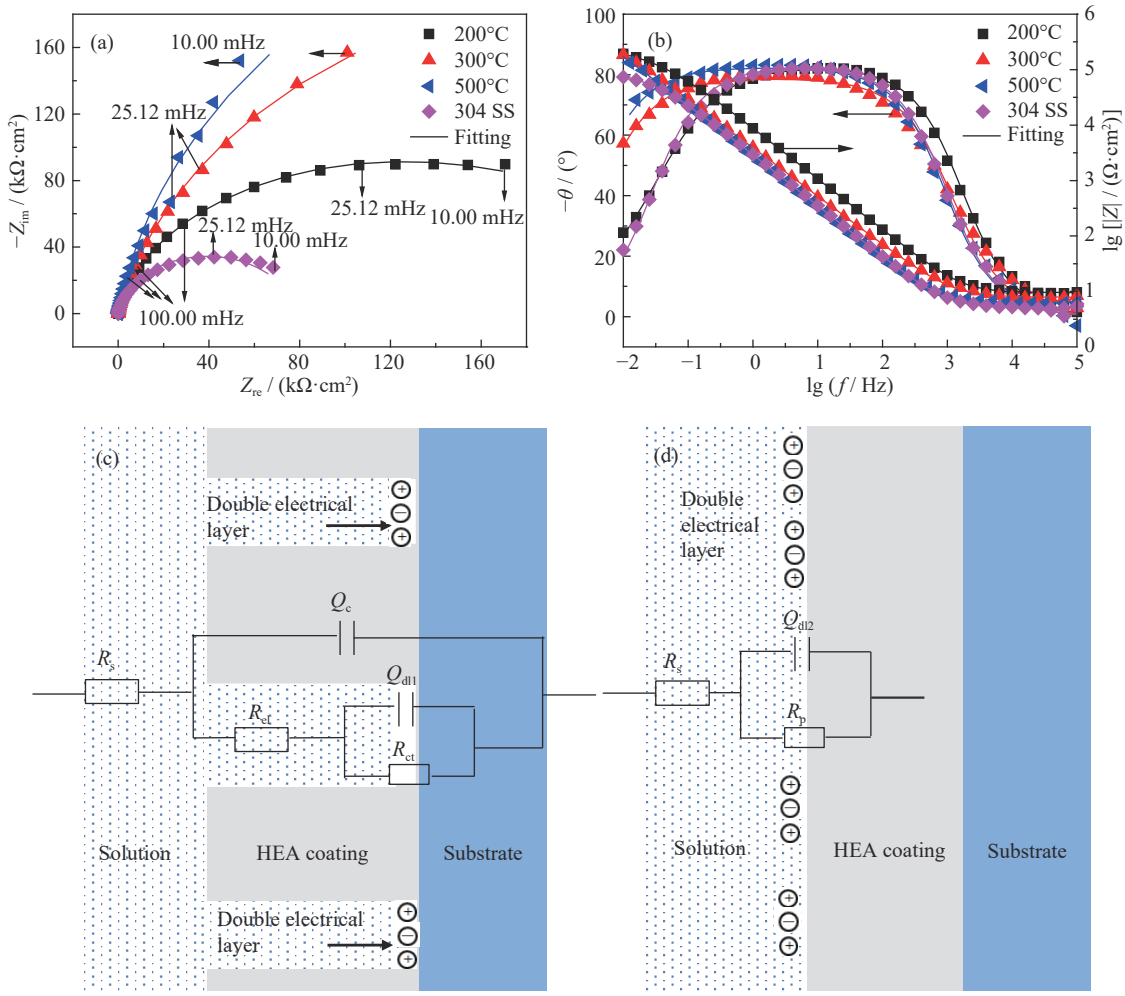

Fig. 4. EIS spectra of the coatings sputtered at 200, 300, and 500°C and that of 304 SS after immersing in 3.5wt% NaCl solution for 3600 s and the EECs: (a) Nyquist plots of the coatings and 304 SS; (b) Bode plots of the coatings and 304 SS; (c) EEC for fitting the EIS results of the coating sputtered at 200°C; (d) EEC for fitting the EIS results of the coatings sputtered at 300 and 500°C and that of 304 SS. Solid lines refer to the fitting curves.

respectively. The value of R_p denotes the protective ability of the coating. The constant phase angle element (CPE, Q) is used to model the capacitance due to the dispersion effect, which is caused by the surface heterogeneity or roughness of the electrode interface [57–59]. Its impedance (Z) was calculated using the following equation:

$$Z = \frac{1}{Y_0 (j\omega)^n} \quad (1)$$

where Y_0 is the CPE constant, n ($0 < n \leq 1$) is the exponent of the CPE, ω is the angular frequency, and j is the imaginary unit.

In this work, the fitting values of the spectra of the coatings sputtered at 200°C and 300 and 500°C are listed in Tables 4 and 5, respectively. As observed from Tables 4 and 5, the resistances of the coatings increased with an increase in the substrate temperature; moreover, the resistance values of all the coatings, i.e., $R_{el} + R_{ct}$ for the coating sputtered at 200°C and R_p for the coatings sputtered at 300 and 500°C, were one order higher than R_p value of the 304 SS substrate. The results revealed that the protective ability and pitting resistance of the coating could be improved by raising the substrate temperature, accordant with the results revealed by po-

Table 4. Fitting values of the elements in the electrical equivalent circuit in Fig. 4(c)

Coating	R_s / (Ω·cm^2)	Q_c		R_{el} /(Ω·cm^2)	Q_{dl1}		R_{ct} / (Ω·cm^2)
		Y_0 / (Ω^{-1}·cm^{-2}·s^n)	n		Y_0 / (Ω^{-1}·cm^{-2}·s^n)	n	
200°C	9.527	2.08×10^{-5}	0.918	1.133×10^5	1.635×10^{-5}	0.462	1.923×10^5

Table 5. Fitting values of the elements in the electrical equivalent circuit in Fig. 4(d)

Coating	R_s / (Ω·cm^2)	Q_{dl2}		R_p / (Ω·cm^2)
		Y_0 / (Ω^{-1}·cm^{-2}·s^n)	n	
300°C	7.836	5.093×10^{-5}	0.876	4.801×10^5
500°C	6.293	6.922×10^{-5}	0.916	6.238×10^5
304 SS	5.107	6.289×10^{-5}	0.920	7.836×10^4

larization curves. Moreover, the results further confirmed that high substrate temperature promotes densification of the coating. The $FeCoCrNiMo_{0.3}$ coating clearly showed an effective protective ability on the 304 SS substrate.

3.3. Effect of deposition time on the thickness and morphology of the coating

On the basis of the aforementioned results, 500°C was selected as the substrate temperature, and the effect of sputtering time (1, 3, and 5 h) on the morphology and corrosion resistance of the coating was investigated. The coatings sputtered for 3 and 5 h still showed the fcc phase (XRD results are not shown here). Fig. 5 shows the cross-sectional and plane-view SEM images of the $FeCoCrNiMo_{0.3}$ coatings sputtered at 500°C for 3 and 5 h. The corresponding EDS results are shown in Figs. 5(e) and 5(f). The chemical composi-

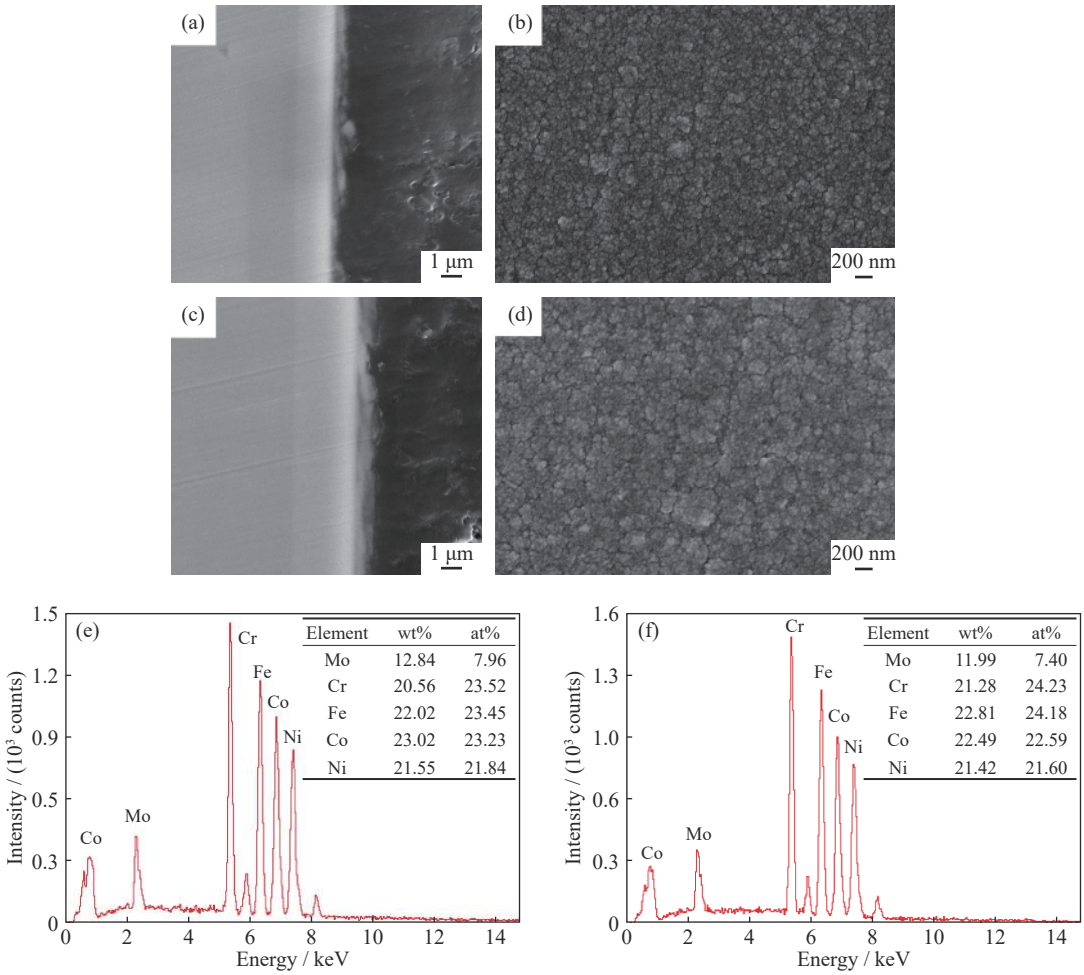

Fig. 5. (a, c) Cross-sectional and (b, d) plane-view SEM images of $FeCoCrNiMo_{0.3}$ coatings sputtered at 500°C for different times and (e, f) the corresponding EDS results of the coatings: (a, b, e) 3 h; (c, d, f) 5 h.

tions of the coatings were approximately the same as those of $FeCoCrNiMo_{0.3}$. The thicknesses of the coatings were (1792 ± 12) and (2996 ± 27) nm, which significantly increased with an increase in sputtering time [60−61].

As shown in Figs. 2(f), 5(b), and 5(d), the island-shaped structure remained on the film surface; moreover, the size of the islands became significantly large as the deposition time increased. An undulating microstructure was also observed and was attributed to the structural zone model [62−63]. The growth of thin films deposited on amorphous or polycrystalline substrates by magnetron sputtering generally follows the Volmer–Weber growth [62]. With an increase in sputtering time, the island coalescence exacerbates. The islands with low energy would merge with others by surface atom diffusion and grain boundary (GB) migration to minimize the surface and interface energy during sputtering, thus resulting in the coarsening of the islands. The temperature would rise as the sputtering time increases further due to continuous bombarding, which in turn accelerates the adatom surface diffusion. GB migration can even take place throughout the film thickening process, as well as during coalescence. Grain coarsening is repeated until the grain size becomes sufficiently large; consequently, the grain boundaries are immobile and the coating with a continuous structure is formed [62−63]. The microstructural evolution controlled by growth processes shows that surface roughness and porosity should gradually decrease with an increase in sputtering time because of sufficient surface diffusion and GB migration [62]. A similar conclusion was obtained in a previous study [38].

3.4. Polarization curves of the coatings sputtered at different times

The corrosion resistance of the $FeCoCrNiMo_{0.3}$ coatings sputtered for different times in 3.5wt% NaCl solution was evaluated by the polarization curves, as shown in Fig. 6. The polarization behaviors of the coatings were similar and exhibited a wide passive region, which indicated excellent pitting resistance. The transpassive dissolution of the coatings occurred at about 1 V vs. SCE, and oxygen evolution occurred above 1.08 mV vs. SCE, according to the E_e−pH diagram [64−65] (E_e: equilibrium potential). E_{corr} and i_{corr} were obtained by Tafel fitting, as listed in Table 6. The i_{corr} value of the coating sputtered for 1 h was slightly high, indicating a high corrosion rate at OCP. Meanwhile, the dissolution rate of the coating sputtered for 1 h was much higher than that of the coatings sputtered for 3 and 5 h in the condition with external potential. The result demonstrated that the pitting resistance and stability of the coating improved by increasing the sputtering time from 1 to 3 h. The result was attributed to the increased thickness and decreased roughness and porosity, as described in Section 3.3. As the sputtering time increased to 5 h, no significant change was observed in the current density relative to that at 3 h. The surface roughness and porosity of the coating sputtered for 5 h did not improve further due to the islands that were fully coalesced after sputtering for 3 h. Therefore, one can conclude that the coatings with optimal thickness and microstructure can completely resist a Cl^- attack after sputtering for 3 h at 500°C.

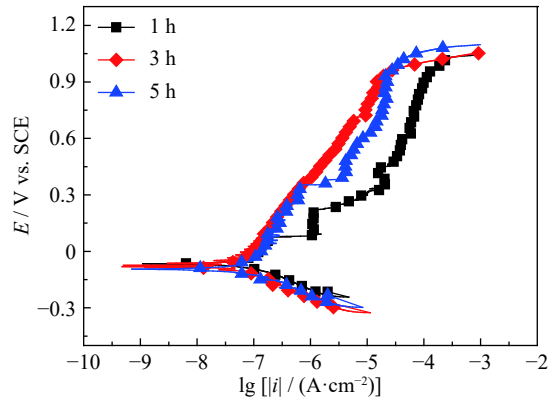

Fig. 6. Dynamic potential polarization curves of the $FeCoCrNiMo_{0.3}$ coatings sputtered for different times in 3.5wt% NaCl solution.

Table 6. Fitting results of polarization curves shown in Fig. 6

Sputtering time / h	E_{corr} / V vs. SCE	i_{corr} / (μA·cm^{-2})
1	–0.0534	0.060
3	–0.0797	0.043
5	–0.0971	0.052

3.5. Comparison of pitting resistances of HEA coatings and bulk HEA alloys

Fig. 7 shows the comparison of the pitting resistances of the $FeCoCrNiMo_{0.3}$ coating in the study and other reported HEA coatings and bulk alloys in 3.5wt% NaCl solution. The pitting potential (E_{pit}) and passive current density (i_{pass}) were used to evaluate the pitting resistance of the coatings and alloys. Fig. 7 shows the AlCrMoNbZr/(AlCrMoNbZr)N multilayer coating [66], CrMnFeCoNi coating [30], VNbMoTaWCrB coating [32], and $AlCoCrFeNiTi_{0.2}$ coating [67]. Other previously reported coatings [68−69] are active or have high i_{pass} values in NaCl solution. Bulk HEA alloys include $Al_xCoCrFeNi$ (x = 0.3, 0.5, 0.7) [70], $FeCoCrNiCu_x$ (x = 0, 0.5, 1) [71], $Co_{0.5}CrCuFeMnNi$ [72], $CoCrFeNiWo_{0.5}Mo_{0.5}$ [68], $Co_{1.5}CrFeNi_{1.5}Ti_{0.5}Mo_{0.1}$ [73], $Ni_{38}Fe_{20}Cr_xMn_{21-0.5x}Co_{21-0.5x}$ (x = 6, 14, 22) (Cr6, Cr14, Cr22) [74], ultrafine-grained (UFG) CoNiFeCrMn [75], and $Ni_{38}Cr_{21}Fe_{20}Ru_{13}Mo_6W_2$ alloys [76]. The pitting resistance of the $FeCoCrNiMo_{0.3}$ coating with high pitting potential was better than that of most HEA coatings and bulk alloys. The elemental compositions of the coating and the investigation about deposition parameters can provide valuable references for the development and preparation of anticorrosion HEA coating. Furthermore, bonding strength and wear resistance should be character-

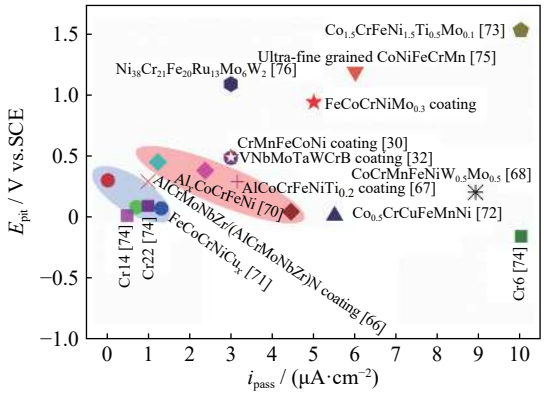

Fig. 7. Comparison of pitting resistance of the $FeCoCrNiMo_{0.3}$ coating in this work and those of other reported HEA coatings and bulk HEA alloys in 3.5wt% NaCl solution.

ized to develop the coating that is applicable to harsh environments.

4. Conclusion

The effects of substrate temperature and sputtering time on the morphologies and corrosion resistance of the coating fabricated by magnetron sputtering were analyzed. A dense coating with remarkably improved pitting resistance and protective property was obtained at a high substrate temperature of 500°C. The thickness of the coating was significantly increased by prolonging the sputtering time. The pitting resistance of the coating sputtered at 500°C for 3 h was better than that sputtered at 1 h. However, it showed no further improvement as the deposition time increased to 5 h. In sum, the $FeCoCrNiMo_{0.3}$ coating sputtered at 500°C exhibited better pitting resistance among the other reported HEA coatings. The result can provide valuable reference for designing and fabricating corrosion-resistant HEA coating subjected to aggressive surroundings.

Acknowledgement

This work was financially supported by the National Science and Technology Major Project of China (No. 2017-VII-0012-0109).

References

[1] B. Ren, S.J. Lv, R.F. Zhao, Z.X. Liu, and S.K. Guan, Effect of sputtering parameters on (AlCrMnMoNiZr)N films, *Surf. Eng.*, 30(2014), No. 2, p. 152.

[2] H. Luo, S.J. Gao, C.F. Dong, and X.G. Li, Characterization of electrochemical and passive behaviour of Alloy 59 in acid solution, *Electrochim. Acta*, 135(2014), p. 412.

[3] A. Pardo, M.C. Merino, A.E. Coy, F. Viejo, R. Arrabal, and E. Matykina, Effect of Mo and Mn additions on the corrosion behaviour of AISI 304 and 316 stainless steels in H_2SO_4, *Corros. Sci.*, 50(2008), p. 780.

[4] C.O.A. Olsson and D. Landolt, Passive films on stainless steels-chemistry, structure and growth, *Electrochim. Acta*, 48(2003), No. 9, p. 1093.

[5] M. Lelis, S. Tuckute, S. Varnagiris, M. Urbonavicius, G. Laukaitis, and K. Bockute, Tailoring of TiO_2 film microstructure by pulsed-DC and RF magnetron co-sputtering, *Surf. Coat. Technol.*, 377(2019), art. No. 124906.

[6] Z. He, S. Zhang, and D. Sun, Effect of bias on structure mechanical properties and corrosion resistance of TiN_x films prepared by ion source assisted magnetron sputtering, *Thin Solid Films*, 676(2019), p. 60.

[7] G. Greczynski, J. Lu, J. Jensen, S. Bolz, W. Kölker, C.H. Schiffers, O. Lemmer, J.E. Greene, and L. Hultman, A review of metal-ion-flux-controlled growth of metastable TiAlN by HIPIMS/DCMS co-sputtering, *Surf. Coat. Technol.*, 257(2014), p. 15.

[8] J.F. Yang, Z.G. Yuan, Q. Liu, X.P. Wang, and Q.F. Fang, Characterization of Mo−Al−N nanocrystalline films synthesized by reactive magnetron sputtering, *Mater. Res. Bull.*, 44(2009), No. 1, p. 86.

[9] U. Jansson and E. Lewin, Sputter deposition of transition-metal carbide films — A critical review from a chemical perspective, *Thin Solid Films*, 536(2013), p. 1.

[10] T.Y. Zhang, J.S. Wu, L. Jin, Z. Zhang, W. Rong, B.W. Zhang, Y. Wang, Y.D. He, W. Liu, and X.G. Li, Enhancing the mechanical and anticorrosion properties of 316L stainless steel via a cathodic plasma electrolytic nitriding treatment with added PEG, *J. Mater. Sci. Technol.*, 35(2019), No. 11, p. 2630.

[11] P.J. Kelly and R.D. Arnell, Magnetron sputtering: A review of recent developments and applications, *Vacuum*, 56(2000), No. 3, p. 159.

[12] J.W. Yeh, S.K. Chen, S.J. Lin, J.Y. Gan, T.S. Chin, T.T. Shun, C.H. Tsau, and S.Y. Chang, Nanostructured high-entropy alloys with multiple principal elements: Novel alloy design concepts and outcomes, *Adv. Eng. Mater.*, 6(2004), No. 5, p. 299.

[13] Y. Zhang, X. Yang, and P.K. Liaw, Alloy design and properties optimization of high-entropy alloys, *JOM*, 64(2012), No. 7, p. 830.

[14] Y. Zhang, T.T. Zuo, Z. Tang, M.C. Gao, K.A. Dahmen, P.K. Liaw, and Z.P. Lu, Microstructures and properties of high-entropy alloys, *Prog. Mater. Sci.*, 61(2014), p. 1.

[15] D.Y. Li, C.X. Li, T. Feng, Y.D. Zhang, G. Sha, J.J. Lewandowski, P.K. Liaw, and Y. Zhang, High-entropy $Al_{0.3}CoCrFeNi$ alloy fibers with high tensile strength and ductility at ambient and cryogenic temperatures, *Acta Mater.*, 123(2017), p. 285.

[16] C.D. Gómez-Esparza, R. Peréz-Bustamante, J.M. Alvarado-Orozco, J. Muñoz-Saldaña, R. Martínez-Sánchez, J.M. Olivares-Ramírez, and A. Duarte-Moller, Microstructural evaluation and nanohardness of an AlCoCuCrFeNiTi high-entropy alloy, *Int. J. Miner. Metall. Mater.*, 26(2019), No. 5, p. 634.

[17] Q.D. Qin, J.B. Qu, Y.J. Hu, Y. Wu, and X. Su, Microstructural characterization and oxidation resistance of multicomponent equiatomic CoCrCuFeNi–TiO high-entropy alloy, *Int. J. Miner. Metall. Mater.*, 25(2018), No. 11, p. 1286.

[18] C.B. Wei, X.H. Du, Y.P. Lu, H. Jiang, T.J. Li, and T.M. Wang, Novel as-cast $AlCrFe_2Ni_2Ti_{0.5}$ high-entropy alloy with excellent mechanical properties, *Int. J. Miner. Metall. Mater.*, 27(2020), No. 10, p. 1312.

[19] X.H. Yan, J.S. Li, W.R. Zhang, and Y. Zhang, A brief review of high-entropy films, *Mater. Chem. Phys.*, 210(2018), p. 12.

[20] H. Can, C.W. Du, C.D. Dai, M. Zheng, Z.Y. Liu, and X.G. Li, Research progress of high-entropy alloy coatings, *Surf. Coat.*,

11(2019), p. 15.
[21] Y. Zhang, T. Han, M. Xiao, and Y. Shen, Effect of process parameters on the microstructure and properties of laser-clad $FeNiCoCrTi_{0.5}$ high-entropy alloy coating, *Int. J. Miner. Metall. Mater.*, 27(2020), p. 630.
[22] W.L. Hsu, H. Murakami, J.W. Yeh, A.C. Yeh, and K. Shimoda, On the study of thermal-sprayed $Ni_{0.2}Co_{0.6}Fe_{0.2}CrSi_{0.2}AlTi_{0.2}$ HEA overlay coating, *Surf. Coat. Technol.*, 316(2017), p. 71.
[23] G. Jin, Z.B. Cai, Y.J. Guan, X.F. Cui, Z. Liu, Y. Li, M.L. Dong, and D. Zhang, High temperature wear performance of laser-cladded FeNiCoAlCu high-entropy alloy coating, *Appl. Surf. Sci.*, 445(2018), p. 113.
[24] W.L. Hsu, Y.C. Yang, C.Y. Chen, and J.W. Yeh, Thermal sprayed high-entropy $NiCo_{0.6}Fe_{0.2}Cr_{1.5}SiAlTi_{0.2}$ coating with improved mechanical properties and oxidation resistance, *Intermetallics*, 89(2017), p. 105.
[25] M.H. Hsieh, M.H. Tsai, W.J. Shen, and J.W. Yeh, Structure and properties of two Al−Cr−Nb−Si−Ti high-entropy nitride coatings, *Surf. Coat. Technol.*, 221(2013), p. 118.
[26] Z.C. Chang, Structure and properties of duodenary (TiVCrZrNbMoHfTaWAlSi)N coatings by reactive magnetron sputtering, *Mater. Chem. Phys.*, 220(2018), p. 98.
[27] S.Y. Lin, S.Y. Chang, Y.C. Huang, F.S. Shieu, and J.W. Yeh, Mechanical performance and nanoindenting deformation of (AlCrTaTiZr)NCy multi-component coatings co-sputtered with bias, *Surf. Coat. Technol.*, 206(2012), No. 24, p. 5096.
[28] P.K. Huang and J.W. Yeh, Inhibition of grain coarsening up to 1000°C in (AlCrNbSiTiV)N superhard coatings, *Scripta Mater.*, 62(2010), No. 2, p. 105.
[29] C.Y. Cheng and J.W. Yeh, High-entropy BNbTaTiZr thin film with excellent thermal stability of amorphous structure and its electrical properties, *Mater. Lett.*, 185(2016), p. 456.
[30] Q.F. Ye, K. Feng, Z.G. Li, F.G. Lu, R.F. Li, J. Huang, and Y.X. Wu, Microstructure and corrosion properties of CrMnFeCoNi high entropy alloy coating, *Appl. Surf. Sci.*, 396(2017), p. 1420.
[31] X.C. Li, Z.Y. Zheng, D. Dou, and J.C. Li, Microstructure and properties of coating of FeAlCuCrCoMn high entropy alloy deposited by direct current magnetron sputtering, *Mater. Res.*, 19(2016), No. 4, p. 802.
[32] S.B. Hung, C.J. Wang, Y.Y. Chen, J.W. Lee, and C.L. Li, Thermal and corrosion properties of V−Nb−Mo−Ta−W and V−Nb−Mo−Ta−W−Cr−B high entropy alloy coatings, *Surf. Coat. Technol.*, 375(2019), p. 802.
[33] S. Zhao, L.X. He, X.X. Fan, C.H. Liu, J.P. Long, L. Wang, H. Chang, J. Wang, and W. Zhang, Microstructure and chloride corrosion property of nanocrystalline AlTiCrNiTa high entropy alloy coating on X80 pipeline steel, *Surf. Coat. Technol.*, 375(2019), p. 215.
[34] S.C. Liang, Z.C. Chang, D.C. Tsai, Y.C. Lin, H.S. Sung, M.J. Deng, and F.S. Shieu, Effects of substrate temperature on the structure and mechanical properties of (TiVCrZrHf)N coatings, *Appl. Surf. Sci.*, 257(2011), No. 17, p. 7709.
[35] X.Y. Sun, X.W. Cheng, H.N. Cai, S. Ma, Z.Q. Xu, and T. Ali, Microstructure, mechanical and physical properties of FeCoNiAlMnW high-entropy films deposited by magnetron sputtering, *Appl. Surf. Sci.*, 507(2020), art. No. 145131.
[36] K. von Fieandt, E.M. Paschalidou, A. Srinath, P. Soucek, L. Riekehr, L. Nyholm, and E. Lewin, Multi-component (Al,Cr,Nb,Y,Zr)N thin films by reactive magnetron sputter deposition for increased hardness and corrosion resistance, *Thin. Solid. Films*, 693(2020), art. No. 137685.
[37] P.K. Huang and J.W. Yeh, Effects of substrate temperature and post-annealing on microstructure and properties of (AlCrNbSiTiV)N coatings, *Thin. Solid. Films*, 518(2009), No. 1, p. 180.
[38] W.B. Liao, S. Lan, L.B. Gao, H.T. Zhang, S. Xu, J. Song, X.L. Wang, and Y. Lu, Nanocrystalline high-entropy alloy (CoCrFeNiAl$_{0.3}$) thin-film coating by magnetron sputtering, *Thin. Solid. Films*, 638(2017), p. 383.
[39] C.Y. Wang, X.N. Li, Z.M. Li, Q. Wang, Y.H. Zheng, Y. Ma, L.X. Bi, Y.Y. Zhang, X.H. Yuan, X. Zhang, C. Dong, and P.K. Liaw, The resistivity–temperature behavior of $Al_xCoCrFeNi$ high-entropy alloy films, *Thin. Solid. Films*, 700(2020), art. No. 137895.
[40] J.B. Lee, Effects of alloying elements, Cr, Mo and N on repassivation characteristics of stainless steels using the abrading electrode technique, *Mater. Chem. Phys.*, 99(2006), No. 2-3, p. 224.
[41] A. Pardo, M.C. Merino, A.E. Coy, F. Viejo, R. Arrabal, and E. Matykina, Pitting corrosion behaviour of austenitic stainless steels – Combining effects of Mn and Mo additions, *Corros. Sci.*, 50(2008), No. 6, p. 1796.
[42] K. Sugimoto and Y. Sawada, Role of alloyed molybdenum in austenitic stainless steels in the inhibition of pitting in neutral halide solutions, *Corrosion*, 32(1976), p. 2940.
[43] M. Liu, X.Q. Cheng, X.G. Li, Y. Pan, and J. Li, Effect of Cr on the passive film formation mechanism of steel rebar in saturated calcium hydroxide solution, *Appl. Surf. Sci.*, 389(2016), p. 1182.
[44] M. Liu, X.X. Cheng, X.G. Li, Z. Jin, and H.X. Liu, Corrosion behavior of Cr modified HRB400 steel rebar in simulated concrete pore solution, *Constr. Build. Mater.*, 93(2015), p. 884.
[45] C.D. Dai, H. Luo, J. Li, C.W. Du, Z.Y. Liu, and J.Z. Yao, X-ray photoelectron spectroscopy and electrochemical investigation of the passive behavior of high-entropy $FeCoCrNiMo_x$ alloys in sulfuric acid, *Appl. Surf. Sci.*, 499(2020), art. No. 143903.
[46] X.L. Shang, Z.J. Wang, Q.F. Wu, J.C. Wang, J.J. Li, and J.K. Yu, Effect of Mo addition on corrosion behavior of high-entropy alloys $CoCrFeNiMo_x$ in aqueous environments, *Acta Metall. Sin.*, 32(2019), No. 1, p. 41.
[47] T.T. Shun, L.Y. Chang, and M.H. Shiu, Age-hardening of the $CoCrFeNiMo_{0.85}$ high-entropy alloy, *Mater. Charact.*, 81(2013), p. 92.
[48] W.H. Liu, Z.P. Lu, J.Y. He, J.H. Luan, Z.J. Wang, B. Liu, Y. Liu, M.W. Chen, and C.T. Liu, Ductile $CoCrFeNiMo_x$ high entropy alloys strengthened by hard intermetallic phases, *Acta Mater.*, 116(2016), p. 332.
[49] Z.F. Wu, X.D. Wang, Q.P. Cao, G.H. Zhao, J.X. Li, D.X. Zhang, J.J. Zhu, and J.Z. Jiang, Microstructure characterization of $Al_xCo_1Cr_1Cu_1Fe_1Ni_{1(x=0 \text{ and } 2.5)}$ high-entropy alloy films, *J. Alloys Compd.*, 609(2014), p. 137.
[50] B.R. Braeckman, F. Boydens, H. Hidalgo, P. Dutheil, M. Jullien, A.L. Thomann, and D. Depla, High entropy alloy thin films deposited by magnetron sputtering of powder targets, *Thin Solid Films*, 580(2015), p. 71.
[51] B.R. Song, Y.H. Li, Z.H. Cong, Y.X. Li, Z.X. Song, and J. Chen, Effects of deposition temperature on the nanomechanical properties of refractory high entropy TaNbHfZr films, *J. Alloys Compd.*, 797(2019), p. 1025.
[52] D.C. Kong, A.N. Xu, C.F. Dong, F.X. Mao, K.X. Xiao, X.G. Li, and D.D. Macdonald, Electrochemical investigation and ab initio computation of passive film properties on copper in anaerobic sulphide solutions, *Corros. Sci.*, 116(2017), p. 34.
[53] M. Isakhani-Zakaria, S.R. Allahkaram, and H.A. Ramezani-Varzaneh, Evaluation of corrosion behaviour of Pb-Co_3O_4 electrodeposited coating using EIS method, *Corros. Sci.*, 157(2019), p. 472.

[54] E. Huttunen-Saarivirta, V.E. Yudin, L.A. Myagkova, and V.M. Svetlichnyi, Corrosion protection of galvanized steel by polyimide coatings: EIS and SEM investigations, *Prog. Org. Coat.*, 72(2011), No. 3, p. 269.

[55] R.M. Fonseca, R.B. Soares, R.G. Carvalho, E.K. Tentardini, V.F.C. Lins, and M.M.R. Castro, Corrosion behavior of magnetron sputtered NbN and $Nb_{1-x}Al_xN$ coatings on AISI 316L stainless steel, *Surf. Coat. Technol.*, 378(2019), art. No. 124987.

[56] T.L. Zhao, Z.Y. Liu, C.W. Du, M.H. Sun, and X.G. Li, Effects of cathodic polarization on corrosion fatigue life of E690 steel in simulated seawater, *Int. J. Fatigue*, 110(2018), p. 105.

[57] Z. Lukács, Evaluation of model and dispersion parameters and their effects on the formation of constant-phase elements in equivalent circuits, *J. Electroanal. Chem.*, 464(1999), No. 1, p. 68.

[58] A. Carnot, I. Frateur, S. Zanna, B. Tribollet, I. Dubois-Brugger, and P. Marcus, Corrosion mechanisms of steel concrete moulds in contact with a demoulding agent studied by EIS and XPS, *Corros. Sci.*, 45(2003), p. 2513.

[59] J.B. Jorcin, M.E. Orazem, N. Pébère, and B. Tribollet, CPE analysis by local electrochemical impedance spectroscopy, *Electrochim. Acta*, 51(2006), No. 8-9, p. 1473.

[60] B. Astinchap, Fractal and statistical characterization of Ti thin films deposited by RF-magnetron sputtering: The effects of deposition time, *Optik*, 178(2019), p. 231.

[61] M. Ahmadipour, M.F. Ain, S. Goutham, and Z.A. Ahmad, Effects of deposition time on properties of $CaCu_3Ti_4O_{12}$ thin film deposited on ITO substrate by RF magnetron sputtering at ambient temperature, *Ceram. Int.*, 44(2018), No. 15, p. 18817.

[62] I. Petrov, P.B. Barna, L. Hultman, and J.E. Greene, Microstructural evolution during film growth, *J. Vac. Sci. Technol. A*, 21(2003), No. 5, p. S117.

[63] S. Mahieu, P. Ghekiere, D. Depla, and R. De Gryse, Biaxial alignment in sputter deposited thin films, *Thin Solid Films*, 515(2006), No. 4, p. 1229.

[64] T. Yamamoto, K. Fushimi, M. Seo, S. Tsuri, T. Adachi, and H. Habazaki, Depassivation–repassivation behavior of type-312L stainless steel in NaCl solution investigated by the micro-indentation, *Corros. Sci.*, 51(2009), No. 7, p. 1545.

[65] Y.J. Kim, S.W. Kim, H.B. Kim, C.N. Park, Y.I. Choi, and C.J. Park, Effects of the precipitation of secondary phases on the erosion-corrosion of 25% Cr duplex stainless steel, *Corros. Sci.*, 152(2019), p. 202.

[66] W. Zhang, M. Wang, L. Wang, C.H. Liu, H. Chang, J.J. Yang, J.L. Liao, Y.Y. Yang, and N. Liu, Interface stability, mechanical and corrosion properties of AlCrMoNbZr/(AlCrMoNbZr)N high-entropy alloy multilayer coatings under helium ion irradiation, *Appl. Surf. Sci.*, 485(2019), p. 108.

[67] J. Liu, H. Liu, P.J. Chen, and J.B. Hao, Microstructural characterization and corrosion behaviour of $AlCoCrFeNiTi_x$ high-entropy alloy coatings fabricated by laser cladding, *Surf. Coat. Technol.*, 361(2019), p. 63.

[68] C.Y. Shang, E.G. Axinte, J. Sun, X.T. Li, P. Li, J.W. Du, P.C. Qiao, and Y. Wang, $CoCrFeNi(W_{1-x}Mo_x)$ high-entropy alloy coatings with excellent mechanical properties and corrosion resistance prepared by mechanical alloying and hot pressing sintering, *Mater. Des.*, 117(2017), p. 193.

[69] Y.K. Shon, S.S. Joshi, S. Katakam, R. Shanker Rajamure, and N.B. Dahotre, Laser additive synthesis of high entropy alloy coating on aluminum: Corrosion behavior, *Mater. Lett.*, 142(2015), p. 122.

[70] Y.Z. Shi, B. Yang, X. Xie, J. Brechtl, K.A. Dahmen, and P.K. Liaw, Corrosion of $Al_xCoCrFeNi$ high-entropy alloys: Al-content and potential scan-rate dependent pitting behavior, *Corros. Sci.*, 119(2017), p. 33.

[71] Y.J. Hsu, W.C. Chiang, and J.K. Wu, Corrosion behavior of $FeCoNiCrCu_x$ high-entropy alloys in 3.5% sodium chloride solution, *Mater. Chem. Phys.*, 92(2005), No. 1, p. 112.

[72] R.F. Zhao, B. Ren, B. Cai, Z.X. Liu, G.P. Zhang, and J.J. Zhang, Corrosion behavior of $Co_xCrCuFeMnNi$ high-entropy alloys prepared by hot pressing sintered in 3.5% NaCl solution, *Results Phys.*, 15(2019), art. No. 102667.

[73] Y.L. Chou, Y.C. Wang, J.W. Yeh, and H.C. Shih, Pitting corrosion of the high-entropy alloy $Co_{1.5}CrFeNi_{1.5}Ti_{0.5}Mo_{0.1}$ in chloride-containing sulphate solutions, *Corros. Sci.*, 52(2010), No. 10, p. 3481.

[74] P. Lu, J.E. Saal, G.B. Olson, T. Li, S. Sahu, O.J. Swanson, G.S. Frankel, A.Y. Gerard, and J.R. Scully, Computational design and initial corrosion assessment of a series of non-equimolar high entropy alloys, *Scripta Mater.*, 172(2019), p. 12.

[75] Z.H. Han, W.N. Ren, J. Yang, A.L. Tian, Y.Z. Du, G. Liu, R. Wei, G. Zhang, and Y.Q. Chen, The corrosion behavior of ultra-fine grained CoNiFeCrMn high-entropy alloys, *J. Alloys Compd.*, 816(2020), art. No. 152583.

[76] T.S. Li, O.J. Swanson, G.S. Frankel, A.Y. Gerard, P. Lu, J.E. Saal, and J.R. Scully, Localized corrosion behavior of a single-phase non-equimolar high entropy alloy, *Electrochim. Acta*, 306(2019), p. 71.